RSC Advances

PAPER

View Article Online
View Journal | View Issue



Cite this: *RSC Adv.*, 2022, **12**, 32365

# Simulation and analysis of lead-free perovskite solar cells incorporating cerium oxide as electron transporting layer

Ali K. Al-Mousoi,[a] Mustafa K. A. Mohammed,*[b] Rahul Pandey,[c] Jaya Madan,[c] Davoud Dastan,[d] G. Ravi,[e] P. Sakthivel[e] and G. Anandha babu[f]

The great demand for renewable energy has greatly contributed to the development of the solar cell industry. Recently, silicon solar cells have dominated the world market. The ease of processing gives perovskite solar cells (PSCs) an advantage over conventional silicon solar cells. Regular silicon photovoltaics require expensive, multi-step processes accomplished in a specialized ultraclean-chamber facility at an elevated temperature (>1000 °C) and highly vacuumed workspace. Hence, researchers and the solar cell industry have focused on PSC as a great rival to silicon solar cells. Despite this, the highest efficiency was obtained from lead-based PSC, which has a considerably high toxicity issue and low stability related to lead content, so the research field pays attention to lead-free perovskite solar cells. In this digital simulation, tin-based perovskite in this paper, methylammonium tin iodide ($MASnI_3$) with the use of cerium oxide ($CeO_x$) as an electron transporting layer (ETL) with varying percentages of oxygen, which means different shallow donor densities (ND). The optimum value for the thickness of the absorber layer (perovskite) was made, and the current–voltage characteristics and efficiency calculations were also accomplished for the best cell. Then an improvement was made by changing the ND value of $CeO_x$, and the best-optimized cell parameters were: open circuit voltage ($V_{OC}$) of 0.92 V, short circuit current density ($J_{SC}$) of 30.79 mA cm$^{-2}$, power conversion efficiency (PCE) of 17.77%, and fill factor (FF) of 62.86%.

Received 21st September 2022
Accepted 27th October 2022

DOI: 10.1039/d2ra05957f

rsc.li/rsc-advances



## 1. Introduction

The production of electricity is crucial for world development and is unquestionably the main driver of economic growth in both industrialized and emerging economies. A huge increase in energy demand is being fueled by both a high population growth rate and increased per capita energy consumption.[1–4] Fossil fuel-based energy sources currently meet the majority of the world's energy needs. However, fossil fuel supplies are being depleted more quickly as energy use rises. Renewable energy solutions must be created in order to address these concerns and the growing need for energy. Solar energy, photovoltaic cells that can be used to convert directly into electricity, is the most abundant renewable energy source.[5–11]

Perovskite has gained popularity as a light-harvesting material for photovoltaic applications. Perovskite has a distinct set of optoelectrical properties, including adjustable band gaps, a high absorption coefficient, long carrier diffusion lengths, and high charge carrier mobilities.[12–16] In 2009, Kojima and colleagues reported a power conversion efficiency (PCE) of 3.8% for perovskite solar cells (PSC).[17] After a decade, Cui *et al.* reported a 20.8% PCE for methylammonium lead iodide PSC.[18] CITY U HK/UW established the most recent approved efficiency of close to 25.8% in 2021.[19] Regardless of the rapid evolution of PCE, the present stability of solar cells makes mass production of PSC difficult.[20–22]

The lead content of lead perovskite solar cells is one of their main disadvantages.[23] Due to lead's toxicity, the Restriction of Hazardous Substances directive of the European Union forbids its use in any electronics or electrical equipment. Alternatives to lead as the metal cation in the perovskite photo-absorber have thus become a significant area of research.[24] Stepping up or down within group IV of the periodic table of elements provides an easy way to replace lead. The recently found element, scarcely radioactively stable flerovium, lies in the row below lead. Due to its radioactivity, it may not be a suitable replacement for lead.[25]

[a]*Department of Radiology and Ultrasonography Techniques, College of Medical Techniques, Al-Farahidi University, 10011 Baghdad, Iraq*

[b]*Radiological Techniques Department, Al-Mustaqbal University College, 51001 Hillah, Babylon, Iraq. E-mail: mustafa_kareem97@yahoo.com*

[c]*VLSI Centre of Excellence, Chitkara University Institute of Engineering and Technology, Chitkara University, 140417 Rajpura, Punjab, India*

[d]*Department of Materials Science and Engineering, Cornell University, Ithaca, NY, 14850, USA*

[e]*Department of Physics, Alagappa University, Karaikudi 630003, Tamil Nadu, India*

[f]*Department of Physics, Bannari Amman Institute of Technology, Tamil Nadu, India*

Due to its lower toxicity, tin (Sn), which is on the same row as lead, would be an excellent replacement for lead in PSCs. Organic tin halide synthesis has been going on for as long as lead halide synthesis.[26] The $MASnI_3$ perovskite, with an energy gap ($E_g$) of 1.3 eV, has been reported to be used in solar cells and produced a PCE of 6.4%. The +2 oxidation state of Sn, which is necessary for the formation of a perovskite, is unstable, and the metal quickly oxidizes to the +4 state when exposed to oxygen or air humidity,[27,28] this affects both the conditions under which the device operates and the technique used to make solar cells. It has only been capable of determining the cell performance of the pure tin halide PSCs with strong sealing of the devices because any interaction with oxygen may instantaneously cause the oxidation of tin.[29]

$CeO_x$ is regarded as one of the most significant infrequent oxides because of its wide bandgap, high dielectric constant, strong ionic conductivity, high thermal and chemical stability, matching lattice parameters with silicon, and exceptional capacity to store and release oxygen.[30,31] Wang *et al.* prepared $CeO_x$ ($x = 1.87$) films by a facile sol–gel approach at a low temperature (150 °C) and used them as an alternative to the high-temperature annealing processed $TiO_2$ ETL. The optimized PSC achieved a champion PCE of 14.32% by adjusting the $CeO_x$ precursor solution.[32] Yang *et al.* used $CeO_x$ as ETL in an inverted structure of PSC, utilizing $CsPbIBr_2$ perovskite as light harvesting material. The all-inorganic PSC recorded a maximum efficiency of 5.6% with improved stability.[33] Jien *et al.* reported $CeO_x$ film as a protection layer for perovskite against humidity and metal reactions with the electrode. The device with $CeO_x$ as the ETL had a PCE of 17.47%.[34]

In this simulation, $CeO_x$ is used as an ETL material due to its tunable broad band gap (3.0–3.6 eV) and outstanding optical and dielectric properties.[35,36] Moreover, $CeO_x$ may enhance the stability of the PSC against moisture and oxygen.[37] A numerical simulation of the solar cell would be necessary to figure out the best set of parameters and the physical parameters for prediction accuracy. The device is simulated using the SCAPS-1 D software and the influence of different properties of the $MASnI_3$ material and $CeO_x$ layer on the efficiency of a tin-PSC is estimated. A unique device structure (fluoride tin oxide (FTO)/$CeO_x$/$MASnI_3$/2,2′,7,7′-tetrakis[*N*,*N*-di(4-ethoxyphenyl)amino]-9,9′-spirobifluorene (Spiro-MeTAD)/Au) of a tin-based PSC using the Spiro-OMeTAD as a hole transporting layer (HTL) has been suggested for modeling. The aim of this simulation is to illustrate that the efficiency of lead-free PSCs may be enhanced by varying the ND value of the $CeO_x$ and the thickness of the absorber layer ($MASnI_3$).

## 2. Architecture and materials properties of suggested PCS

For PV modelling, a one-dimensional SCAPS simulation software was employed. The SCPAS program employs Poisson's equation, which defines the relationship between the photocarrier and the semiconductor's electrostatic potential, and continuity equations, which represent charge generation and recombination kinetics in materials.[38] Solving both Poisson's equation and the continuity equation gives us the QE and *J*–*V* properties.[39] Using Poisson's equation and the continuity equation, it is possible to figure out the density of electrons and holes.[40] Poisson's equation can be used to determine the distribution of the electric field $E(x)$:

$$\frac{dE}{dx} = \frac{\rho}{\varepsilon}, \quad \rho(x) = q(N_D + p - N_A - n)$$

Drift and diffusion current densities control the transportation properties of charge carriers in semiconductor. The following equations describe the drift and diffusion current densities for electrons and holes.[38]

$$J_n = qn(x)\mu_n E(x) + qD_n \frac{dn}{dx}$$

$$J_p = qp(x)\mu_p E(x) - qD_p \frac{dp}{dx}$$

where $\mu_n$ and $\mu_p$ are to electron hole mobility, respectively, and $D_n$, and $D_p$ are electron and hole diffusion coefficients respectively. $\rho(x)$, $\varepsilon$, and $q$ refer to space charge distribution, dielectric permittivity, and charge of electron, respectively. $n(x)$ and $J_n$ represent the concentration and current density of electrons. $p(x)$ and $J_p$ represent the concentration and current density of hole. Seven layers, consisting of perovskite absorber, ETL, HTL, and electrodes, can be constructed into a HPSC using the SCAPS software. All PV computations in this study are performed under AM 1.5G (100 mW $cm^{-2}$) conditions.

The structure for the proposed PSC, FTO/$CeO_x$/$MASnI_3$/Spiro-OMeTAD/Au, is shown in Fig. 1a. The FTO layer, which is deposited on a glass substrate, acts as a front transparent contact. The $CeO_x$ layer represents the crucial layer that determines the performance of the device since the transport of electrons is a major factor affecting the PCE. $MASnI_3$ perovskite is the absorber material that is responsible for charge carrier generation through light absorption. Spiro-OMeTAD material acts as HTL. The energy band graph of the suggested structure (Fig. 1b) clearly shows that the conduction bands of the absorbing material $MASnI_3$ are smaller than those of electron transporting material $CeO_x$, and the mismatch between the conduction band (CB) of $MASnI_3$ and the $CeO_x$ material is very slight. As a direct consequence, electrons can easily pass from $MASnI_3$ to FTO *via* $CeO_x$. Electrons can thus move freely through $CeO_x$ from $MASnI_3$ to FTO. A very large valence band (VB) offset (VBO) exists between the absorbing material $MASnI_3$ and the ETL material $CeO_x$. Therefore, the positive charge ($h^+$) in the ETL material $CeO_x$ will be sealed. As shown in Fig. 1b, the valence bands of the hole transporting material Spiro-OMeTAD are greater than those of the absorbing material $MASnI_3$, and the valence band mismatch among those two materials is significantly small. Furthermore, the offsetting in the conduction bands between the HTL material Spiro-OMeTAD and the absorbing material $MASnI_3$ is very considerable, forbidding the electrons from $MASnI_3$ from reaching the back contact.

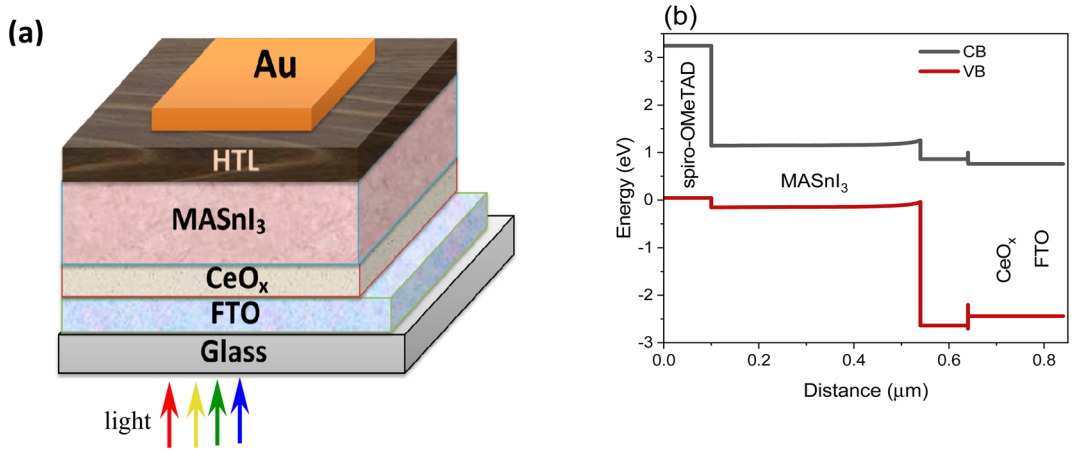


Fig. 1 (a) Schematic layout of the designed PSC and (b) energy bands graph of the PSC.

Table 1 Physical parameters of FTO/$CeO_x$/$MASnI_3$/Spiro-OMeTAD/Au device

| Material | Spiro-OMeTAD | $MASnI_3$ | $CeO_x$ | FTO |
|---|---|---|---|---|
| Thickness of layer (μm) | 0.1 | 0.44 | 0.1 | 0.2 |
| Energy band gab (eV) | 3.2 | 1.3 | 3.5 | 3.2 |
| Electron affinity (eV) | 2.1 | 4.2 | 4.6 | 4.4 |
| Relative permittivity | 3 | 10 | 9 | 9 |
| CB effective densities of states ($cm^{-3}$) | $2.50 \times 10^{18}$ | $1 \times 10^{18}$ | $1 \times 10^{20}$ | $2.2 \times 10^{18}$ |
| VB effective densities of states ($cm^{-3}$) | $1.8 \times 10^{19}$ | $1 \times 10^{18}$ | $2 \times 10^{21}$ | $1.8 \times 10^{19}$ |
| Electron thermal velocity (cm $s^{-1}$) | $1 \times 10^{7}$ | $1 \times 10^{7}$ | $1 \times 10^{7}$ | $1 \times 10^{7}$ |
| Hole thermal velocity (cm $s^{-1}$) | $1 \times 10^{7}$ | $1 \times 10^{7}$ | $1 \times 10^{7}$ | $1 \times 10^{7}$ |
| Mobility of electron ($cm^2$ $V^{-1}$ $s^{-1}$) | $2 \times 10^{4}$ | 1.6 | 100 | 20 |
| Mobility of hole ($cm^2$ $V^{-1}$ $s^{-1}$) | $2 \times 10^{4}$ | 1.6 | 25 | 10 |
| Uniform donor densities ND ($cm^{-3}$) | — | — | $1 \times 10^{21}$ | $1 \times 10^{21}$ |
| Uniform acceptor densities NA ($cm^{-3}$) | $1 \times 10^{20}$ | $3.20 \times 10^{15}$ | — | — |
| Defect | $1 \times 10^{14}$ | $4.5 \times 10^{16}$ | $1 \times 10^{15}$ | $1 \times 10^{15}$ |

Table 2 Interface parameters of FTO/$CeO_x$/$MASnI_3$/Spiro-OMeTAD/Au PSC

| Parameters | Spiro-OMeTAD/$MASnI_3$ interface | $CeO_x$/$MASnI_3$ interface |
|---|---|---|
| Defects type | Neutral | Neutral |
| Capture cross-section for electron ($cm^2$) | $1 \times 10^{-19}$ | $1 \times 10^{-19}$ |
| Capture cross-section for hole ($cm^2$) | $1 \times 10^{-19}$ | $1 \times 10^{-19}$ |
| Energetic distributions | Single | Single |
| Defects energy level $E_t$ | Up the maximum $E_v$ | Up the maximum $E_v$ |
| Reference for defect energy level $E_t$ | 0.06 | 0.06 |
| Total density (integrated over all energies) ($cm^{-2}$) | $1 \times 10^{10}$ | $1 \times 10^{10}$ |

The physical parameters for the simulations of the FTO/$CeO_x$/$MASnI_3$/Spiro-OMeTAD/Au heterostructure solar cell are listed in Table 1,[41] whereas the physical properties of the defects density in $MASnI_3$ are listed in Table 2. All simulations are achieved at a temperature of 300 K.

## 3. Results and discussion

### 3.1 Optimization of $MASnI_3$ thickness

The thickness of the absorbing material plays a significant role in solar cell efficiency since it is related to the absorption of the incident light, which leads to enhancing the *I–V* characteristics.[42–44] In this study, all the parameters of the materials in Tables 1 and 2 are kept fixed, and different values of the thickness of $MASnI_3$ are selected in order to estimate the optimum thickness value of the absorber material. Fig. 2 shows the parameters of the suggested PSC as a function of $MASnI_3$ thickness. As Fig. 2a illustrates the quantum efficiency of the suggested PSC, we can see the influence of the absorbing material thickness on the QE value. As expected, by increasing the value of the thickness, the QE value increases. Fig. 2b demonstrates the *J–V* curve of the PSC under the illumination of 100 mW $cm^{-2}$ (air mass AM 1.5G). Fig. 2c–f shows the $V_{OC}$, $J_{SC}$, FF, and, PCE respectively. From Fig. 2b, the $V_{OC}$ is slightly decreased with thickness increases, while Fig. 2c shows a significant change in the value of $J_{SC}$. Besides the variant $J_{SC}$

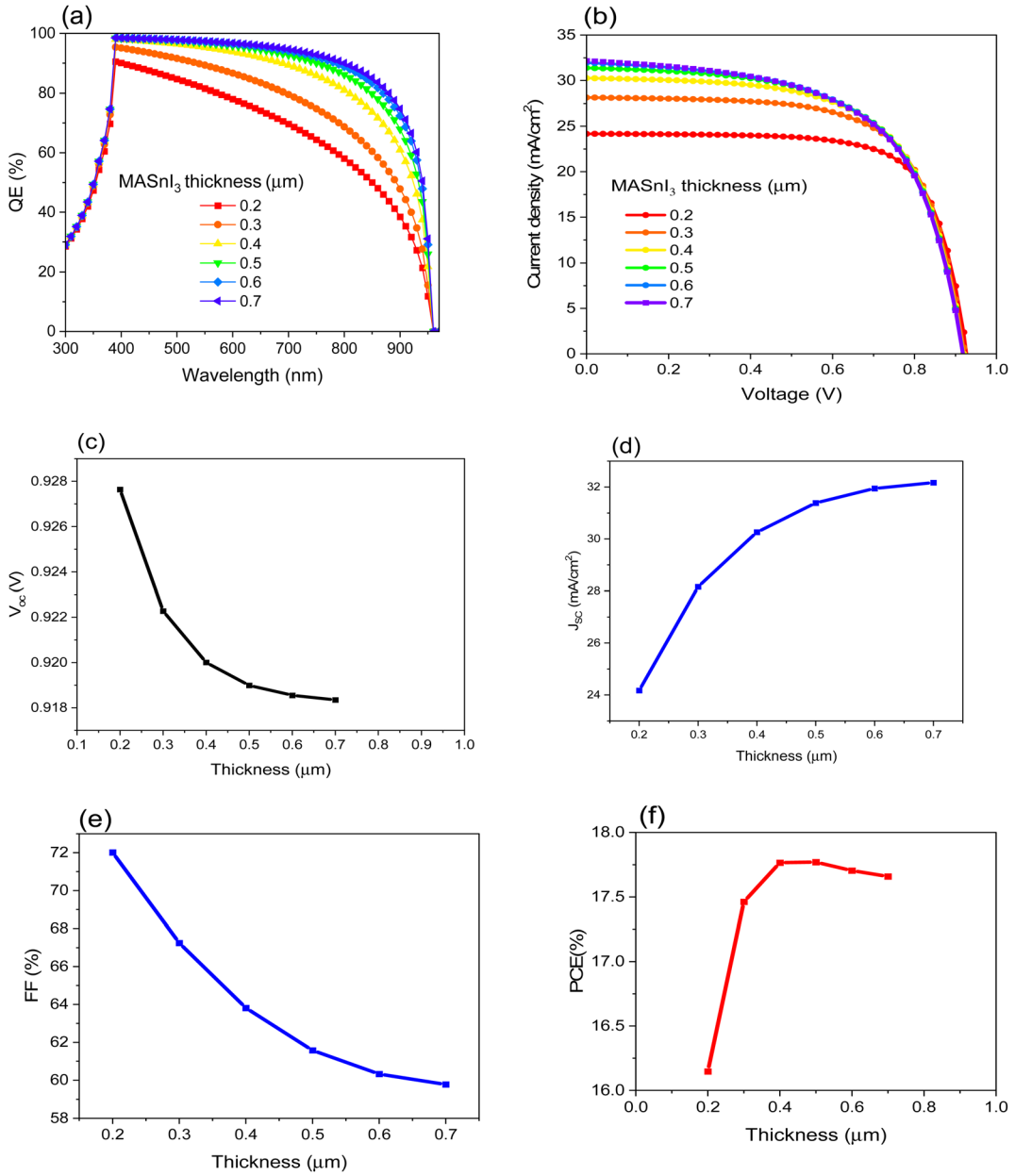


Fig. 2 . Displays the impact of the $MASnI_3$ thickness on the efficiency of FTO/$CeO_x$/$MASnI_3$/Spiro-OMeTAD/Au PSC where (a) QE, (b) *J*–*V* curve, (c) $V_{OC}$, (d) $J_{SC}$, (e) FF and (f) PCE.

with the thickness of the absorbing material, the FF is also highly affected by the thickness, as shown in Fig. 2d. As a consequence of the change in the last mentioned parameters, the PCE varies with changing the thickness, as illustrated in Fig. 2e. Table 3 shows the calculated parameters that are used to select the optimum thickness.

Table 3 Parameters of FTO/$CeO_x$/$MASnI_3$/Spiro-OMeTAD/Au PSC with different thickness of $MASnI_3$

| $MASnI_3$ thickness (μm) | $V_{OC}$ (V) | $J_{SC}$ (mA cm$^{-2}$) | FF (%) | PCE (%) | $V_m$ (V) | $J_m$ (mA cm$^{-2}$) |
|---|---|---|---|---|---|---|
| 0.2 | 0.928 | 24.172 | 72.010 | 16.147 | 0.754 | 21.406 |
| 0.3 | 0.922 | 28.158 | 67.243 | 17.463 | 0.726 | 24.056 |
| 0.4 | 0.920 | 30.260 | 63.815 | 17.766 | 0.711 | 24.993 |
| 0.5 | 0.919 | 31.386 | 61.573 | 17.770 | 0.704 | 25.217 |
| 0.6 | 0.919 | 31.948 | 60.327 | 17.703 | 0.702 | 25.218 |
| 0.7 | 0.918 | 32.169 | 59.776 | 17.659 | 0.701 | 25.185 |

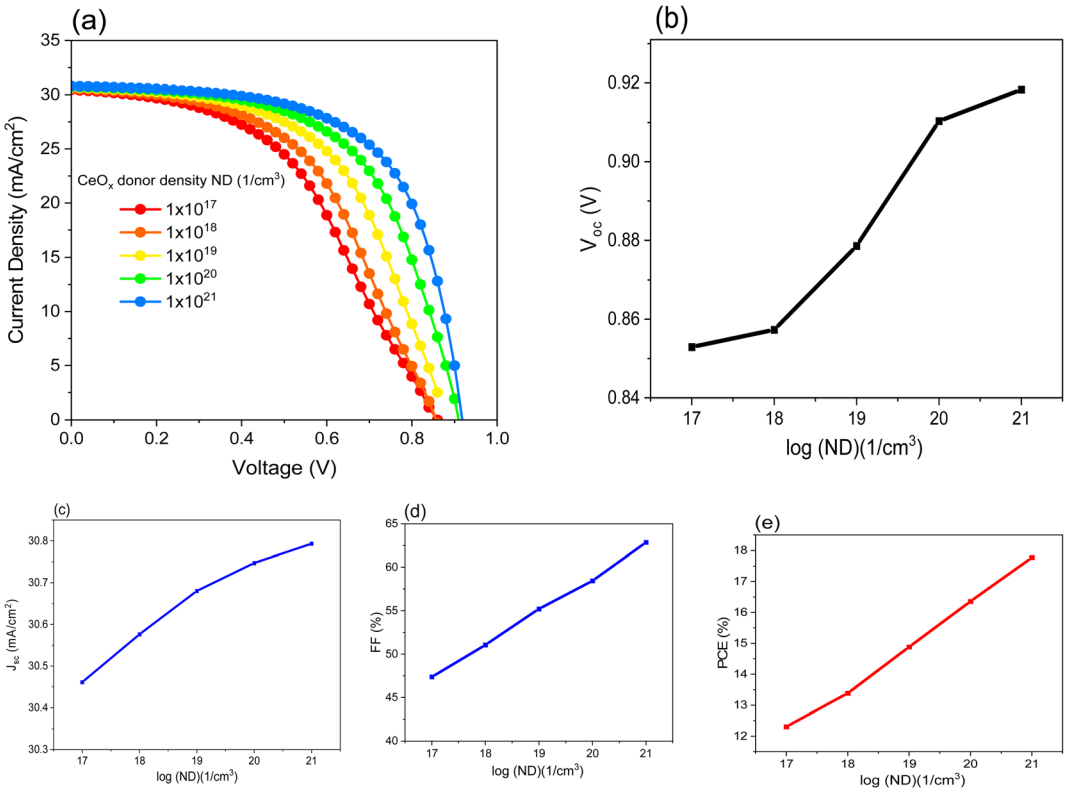


Fig. 3 Shows the effect of the ND of $CeO_x$ on performance of FTO/$CeO_x$/$MASnI_3$/Spiro-OMeTAD/Au PSC where: (a) ($J$–$V$) curve, (b), (c) $J_{SC}$, (d) FF and (e) PCE.

### 3.2 Optimization of donor density (ND) of the $CeO_x$

The percentage of oxygen content in $CeO_x$ determines the value of ND.[45] In this simulation, different values of ND are chosen in order to understand their effect on the PSC performance. Fig. 3a–e shows the variation of the solar cell parameters as a function of log(ND). All the parameter values increase as the value of ND increases. This is attributed to the enhancement of the conductivity, which makes the movement of the electrons through the ETL much easier. ETL's primary function is to give electrons a low-resistive route so that they can be collected. Additionally, it must prevent electrons from stacking up close to the interface. On the other hand, if this happens because of lower conductivity, unrestricted electrons and holes interact together on the interfacial side, resulting in a decreased generated current. Low conductivity causes a higher series resistance ($R_s$). The high value of resistance in the cell causes the FF to drop. The influence of low conductivity in this case caused by low ND will affect both the FF and $V_{OC}$, as shown in Fig. 3b and d, while the $J_{SC}$ is not significantly influenced. Table 4 summarizes the obtained results when varying the ND value. It is obvious that the best PCE obtained of 17.77% at ND is equal to $1 \times 10^{21}$ $cm^{-3}$. As the ND of $CeO_x$ increases to a certain point, the PCE also increases. After this point, the ND of the cerium oxide has no effect on the PCE because the $CeO_x$ has degenerated (practically). Furthermore, once the ND reaches a certain value where the $CeO_x$ serves as a hole-blocking and electron-transporting layer, any further increase in the ND value is unnecessary.[46]

### 3.3 Effect of the series and shunt resistance ($R_s$ & $R_{sh}$)

The $R_s$ and $R_{sh}$ have significant control over how well solar cells work. It comes from the metal connections on the solar cell and layer surfaces. The device's efficiency was assessed by changing the value of $R_s$ from 0 to 10 (Ω $cm^2$). Fig. 4a–d show that as $R_s$ increases, the FF and PCE decrease, resulting in leakage currents, while the $V_{OC}$ and $J_{SC}$ remain unchanged.

Table 4 Parameters of FTO/$CeO_x$/$MASnI_3$/Spiro-OMeTAD/Au PSC with differt values of ND of $CeO_x$

| ND ($cm^{-3}$) | $V_{OC}$ (V) | $J_{SC}$ (mA $cm^{-2}$) | FF (%) | PCE (%) | $V_m$ (V) | $J_m$ (mA $cm^{-2}$) |
|---|---|---|---|---|---|---|
| $1 \times 10^{17}$ | 0.85 | 30.46 | 47.37 | 11.82 | 0.52 | 23.58 |
| $1 \times 10^{18}$ | 0.86 | 30.58 | 51.07 | 13.37 | 0.56 | 24.05 |
| $1 \times 10^{19}$ | 0.88 | 30.68 | 55.21 | 14.87 | 0.61 | 24.49 |
| $1 \times 10^{20}$ | 0.91 | 30.75 | 58.45 | 16.35 | 0.66 | 24.83 |
| $1 \times 10^{21}$ | 0.92 | 30.79 | 62.86 | 17.77 | 0.71 | 25.13 |

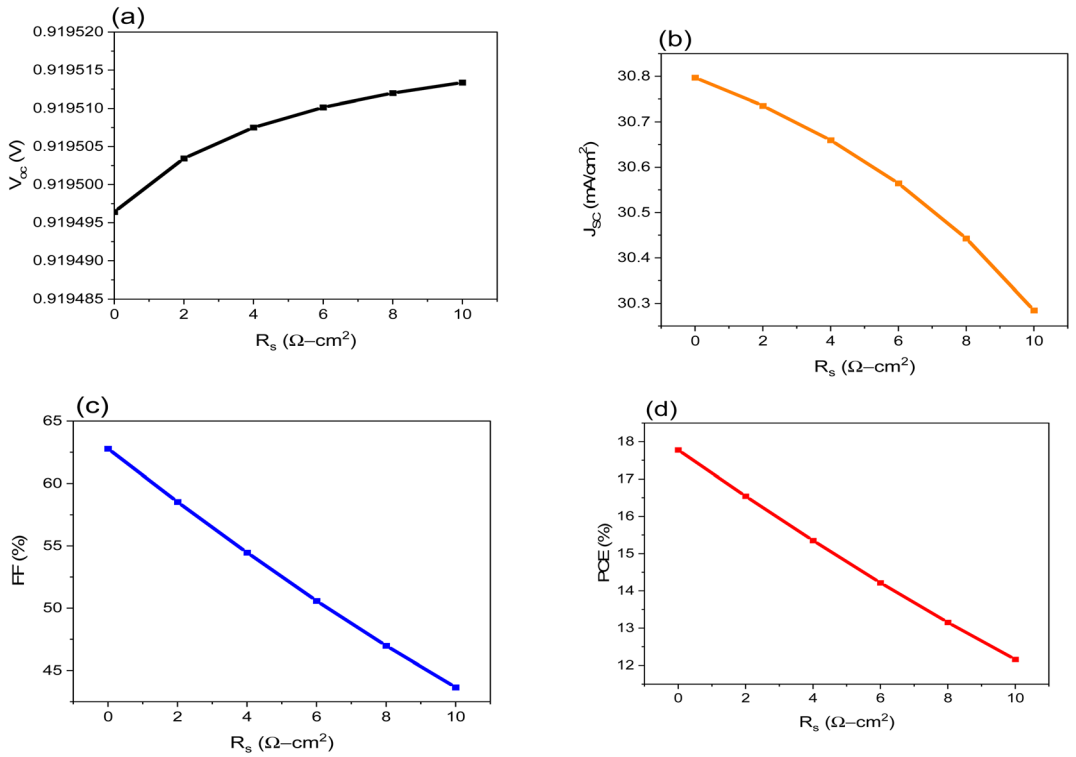


Fig. 4 Shows the influence of $R_s$ on the performance of FTO/$CeO_x$/$MASnI_3$/Spiro-OMeTAD/Au PSC where: (a) $V_{OC}$, (b), $J_{SC}$, (c) FF and (d) PCE.

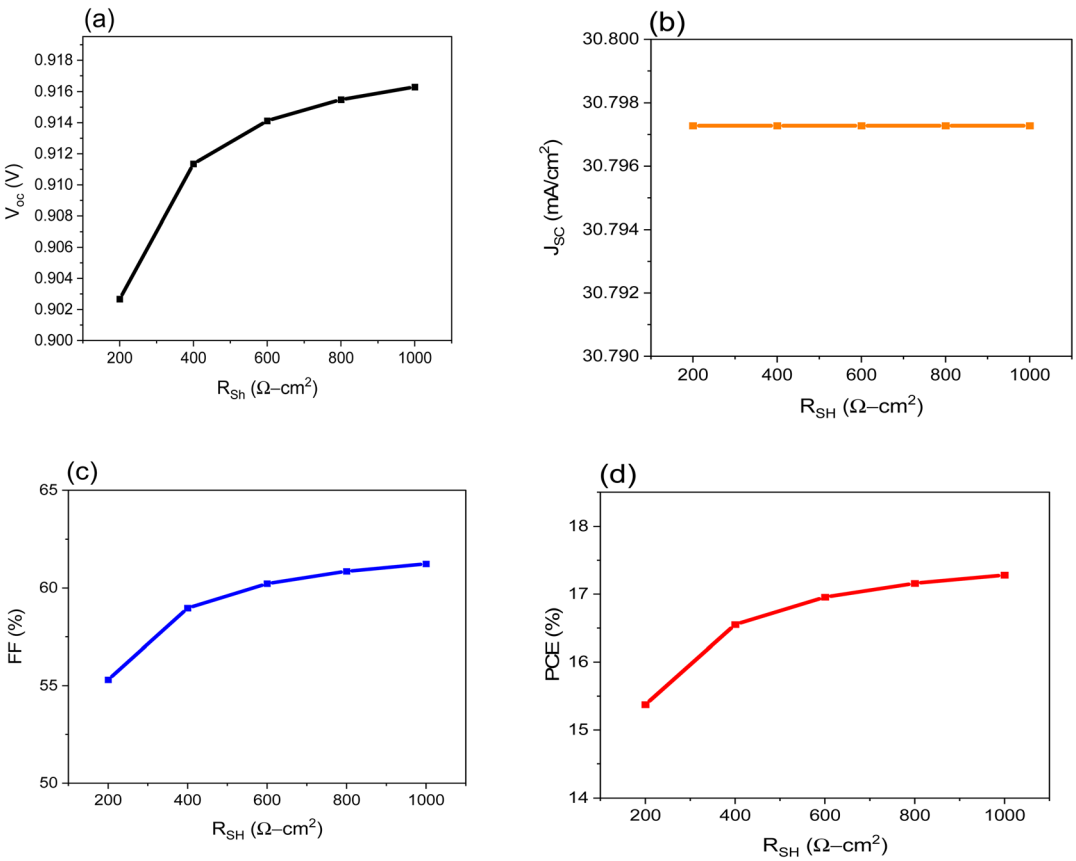


Fig. 5 Shows the impact of $R_{sh}$ of the on performance of FTO/$CeO_x$/$MASnI_3$/Spiro-OMeTAD/Au PSC where: (a) $V_{OC}$, (b), $J_{SC}$, (c) FF and (d) PCE.

Table 5 A comparison between our work and previously published studies used $CeO_x$ As an ETL

| Author | Structure | Perovskite thickness (nm) | Total defect density ($cm^{-3}$) | PCE (%) |
|---|---|---|---|---|
| Anu *et al.*[47] | FTO/$CeO_x$/PCBM/$MAPbI_3$/Spiro-OMeTAD/Au | 250 | $5 \times 10^{14}$ | 18.36 |
| Pandey *et al.*[45] | FTO/$CeO_x$/PCBM/$MAPbI_3$/CNTs/Spiro-OMeTAD/Ag | 250 | $2.14 \times 10^{17}$ | 18.20 |
| Raoui *et al.*[48] | FTO/$CeO_x$/PCBM/$CsSn_{0.5}Ge_{0.5}I_3$/PTAA/Spiro-OMeTAD/Au | 200 | $1 \times 10^{11}$ | 24.20 |
| Ahmmed *et al.*[49] | ITO/$CeO_x$/$CsBi_3I_{10}$/$NiO_x$/Au | 1000 | $1 \times 10^{14}$ | 19.16 |
| Moiz *et al.*[50] | FTO/$CeO_x$/$Cs_2TiBr_6$/*N*,*N*′-bis(naphthalen-1-yl)-*N*,*N*′-bis(phenyl)-benzidine/Au | 150 | $1 \times 10^{15}$ | 20.40 |
| This work | FTO/$CeO_x$/$MASnI_3$/Spiro-OMeTAD/Au | 600 | $4.5 \times 10^{16}$ | 17.77 |

Poor shunt resistance increases power loss in the solar cell by enabling the current produced by light to take an alternative path. A similar deflection drops the voltage produced by the photovoltaic cell and minimizes the current flowing through the photovoltaic junction. Fig. 5a–d shows that the FF is the most affected parameter, resulting in a decrease in the value of PCE, while the $V_{OC}$ and $J_{SC}$ are almost unchanged.

Notably, the results showed that PSCs designed with a room-temperature $CeO_x$ layer could improve the PCE of $MASnI_3$-based photovoltaics, which is a significant step toward PSC industrialization. Table 5 shows the results of a comparison between the various structures, and it can be stated that adding $CeO_x$ into the perovskite-based devices is the most beneficial method for using it in PSCs.

## 4. Conclusions

The performance of the suggested cell structure FTO/$CeO_x$/$MASnI_3$/Spiro-OMeTAD/Au PSC has been examined using the SCAPS 1D simulation software. Different $CeO_x$ and $MASnI_3$ parameters are tuned in order to investigate the behavior of the device. The open-circuit voltage and efficiency received a significant contribution from the $CeO_x$ layer. Cell performance was shown to be enhanced by the $CeO_x$ ETL's higher ND. Cell performance appears to be significantly influenced by the $MASnI_3$ layer's thickness. The density of the $MASnI_3$/$CeO_x$/$MASnI_3$ interfacial defect and the $MASnI_3$/Spiro-OMeTAD interfacial defect were determined. The highest PCE ever calculated was 17.77%, with a $J_{SC}$ value of 30.79 mA $cm^{-2}$, a $V_{OC}$ value of 0.919 V, and a fill factor of 62.78%. Our findings indicate that future research may show that the suggested device structure involving both $CeO_x$ and $MASnI_3$ is an effective device for making thin-film solar cells that are both inexpensive and efficient.

## Data availability

Data will be available based on reasonable request.

## Ethics approval and consent to participate

We comply with the ethical standards. We provide our consent to take part.

## Conflicts of interest

There are no conflicts to declare.

## References

1 K. Brinkmann, T. Becker, F. Zimmermann, C. Kreusel, T. Gahlmann, M. Theisen, T. Haeger, S. Olthof, C. Tückmantel and M. Günster, Perovskite–organic tandem solar cells with indium oxide interconnect, *Nature*, 2022, **604**(7905), 280–286.
2 Y. Ding, B. Ding, H. Kanda, O. J. Usiobo, T. Gallet, Z. Yang, Y. Liu, H. Huang, J. Sheng and C. Liu, Single-crystalline $TiO_2$ nanoparticles for stable and efficient perovskite modules, *Nat. Nanotechnol.*, 2022, 1–8.
3 R. York and S. E. Bell, Energy transitions or additions?: why a transition from fossil fuels requires more than the growth of renewable energy, *Energy Res. Social Sci.*, 2019, **51**, 40–43.
4 A. J. Chapman, B. C. McLellan and T. Tezuka, Prioritizing mitigation efforts considering co-benefits, equity and energy justice: fossil fuel to renewable energy transition pathways, *Appl. Energy*, 2018, **219**, 187–198.
5 K. A. S. Singh, M. K. Mohammed and A. E. Shalan, Effect of 2D perovskite layer and multivalent defect on the performance of 3D/2D bilayered perovskite solar cells through computational simulation studies, *Solar Energy*, 2021, **223**, 193–201.
6 A. Al-Mousoi, M. Mehde and A. Al-Gebori, Annealing temperature effects on the performance of the perovskite solar cells, *IOP Conference Series: Materials Science and Engineering*, IOP Publishing, 2020, p. 012039.
7 M. K. Mohammed and A. K. Al-Mousoi, Deposition of multi-layer graphene (MLG) film on glass slide by flame synthesis technique, *Optik*, 2016, **127**(20), 9848–9852.
8 J.-P. Correa-Baena, M. Saliba, T. Buonassisi, M. Grätzel, A. Abate, W. Tress and A. J. S. Hagfeldt, Promises and challenges of perovskite solar cells, *Science*, 2017, **358**(6364), 739–744.
9 M. D. Humadi, H. T. Hussein, M. S. Mohamed, M. K. Mohammed and E. Kayahan, A facile approach to improve the performance and stability of perovskite solar cells *via* FA/MA precursor temperature controlling in sequential deposition fabrication, *Opt. Mater.*, 2021, **112**, 110794.

10 M. J. Kadhim and M. K. Mohammed, Fabrication of Efficient Triple-Cation Perovskite Solar Cells Employing Ethyl Acetate as an Environmental-Friendly Solvent Additive, *Mater. Res. Bull.*, 2022, 112047.

11 M. K. Mohammed, A. K. Al-Mousoi, S. M. Majeed, S. Singh, A. Kumar, R. Pandey, J. Madan, D. S. Ahmed and D. Dastan, Stable Hole-Transporting Material-Free Perovskite Solar Cells with Efficiency Exceeding 14% *via* the Introduction of a Malonic Acid Additive for a Perovskite Precursor, *Energy Fuel.*, 2022, **36**(21), 13187–13194.

12 S. H. Kareem, M. H. Elewi, A. M. Naji, D. S. Ahmed and M. K. Mohammed, Efficient and stable pure α-phase $FAPbI_3$ perovskite solar cells with a dual engineering strategy: additive and dimensional engineering approaches, *Chem. Eng. J.*, 2022, 136469.

13 M. K. Mohammed, M. S. Jabir, H. G. Abdulzahraa, S. H. Mohammed, W. K. Al-Azzawi, D. S. Ahmed, S. Singh, A. Kumar, S. Asaithambi and M. Shekargoftar, Introduction of cadmium chloride additive to improve the performance and stability of perovskite solar cells, *RSC Adv.*, 2022, **12**(32), 20461–20470.

14 M. M. Moharam, A. N. El Shazly, K. V. Anand, D. E. Rayan, M. K. Mohammed, M. M. Rashad and A. E. Shalan, Semiconductors as effective electrodes for dye sensitized solar cell applications, *Top. Curr. Chem.*, 2021, **379**(3), 1–17.

15 A. K. Al-Mousoi and M. K. Mohammed, Engineered surface properties of MAPI using different antisolvents for hole transport layer-free perovskite solar cell (HTL-free PSC), *J. Sol-Gel Sci. Technol.*, 2020, **96**(3), 659–668.

16 M. K. Mohammed, A. K. Al-Mousoi, S. Singh, U. Younis, A. Kumar, D. Dastan and G. Ravi, Ionic Liquid Passivator for Mesoporous Titanium Dioxide Electron Transport Layer to Enhance the Efficiency and Stability of Hole Conductor-Free Perovskite Solar Cells, *Energy Fuel.*, 2022, **36**(19), 12192–12200.

17 A. Kojima, K. Teshima, Y. Shirai and T. Miyasaka, Organometal halide perovskites as visible-light sensitizers for photovoltaic cells, *J. Am. Chem. Soc.*, 2009, **131**(17), 6050–6051.

18 P. Cui, D. Wei, J. Ji, H. Huang, E. Jia, S. Dou, T. Wang, W. Wang and M. J. N. E. Li, Planar p–n homojunction perovskite solar cells with efficiency exceeding 21.3%, *Nat. Energy*, 2019, **4**(2), 150–159.

19 H. Min, D. Y. Lee, J. Kim, G. Kim, K. S. Lee, J. Kim, M. J. Paik, Y. K. Kim, K. S. Kim and M. G. J. N. Kim, Perovskite solar cells with atomically coherent interlayers on $SnO_2$ electrodes, *Nature*, 2021, **598**(7881), 444–450.

20 M. S. Mehde, A. M. Al-Gebori and A. K. Hantoosh, The effect of the spinning speed variation on the perovskite solar cell efficiency, *IOP Conference Series: Materials Science and Engineering*, IOP Publishing, 2020, p. 012071.

21 M. K. Mohammed, A. K. Al-Mousoi, M. S. Mehde and A. M. Al-Gebori, Engineered electronic properties of the spin-coated MAPI for hole-transport-free perovskite solar cell (HT-free PSC): spinning time and PSC performance relationship, *Chem. Phys. Lett.*, 2020, **754**, 137718.

22 D. S. Ahmed, B. K. Mohammed and M. K. Mohammed, Long-term stable and hysteresis-free planar perovskite solar cells using green antisolvent strategy, *J. Mater. Sci.*, 2021, **56**(27), 15205–15214.

23 J. Cao, F. J. E. Yan and E. Science, Recent progress in tin-based perovskite solar cells, *Energy Environ. Sci.*, 2021, **14**(3), 1286–1325.

24 G. Schileo and G. Grancini, Lead or no lead? Availability, toxicity, sustainability and environmental impact of lead-free perovskite solar cells, *J. Mater. Chem. C*, 2021, **9**(1), 67–76.

25 S. F. Hoefler, G. Trimmel and T. Rath, Progress on lead-free metal halide perovskites for photovoltaic applications: a review, *Monatshefte für Chemie-Chemical Monthly*, 2017, **148**(5), 795–826.

26 N. Sun, W. Gao, H. Dong, Y. Liu, X. Liu, Z. Wu, L. Song, C. Ran and Y. Chen, Architecture of pin Sn-based perovskite solar cells: characteristics, advances, and perspectives, *ACS Energy Lett.*, 2021, **6**(8), 2863–2875.

27 X. Liu, Z. Yang, C.-C. Chueh, A. Rajagopal, S. T. Williams, Y. Sun and A. Jen, Improved efficiency and stability of Pb–Sn binary perovskite solar cells by Cs substitution, *J. Mater. Chem. A*, 2016, **4**(46), 17939–17945.

28 M. E. Kayesh, K. Matsuishi, R. Kaneko, S. Kazaoui, J.-J. Lee, T. Noda and A. J. A. E. L. Islam, Coadditive engineering with 5-ammonium valeric acid iodide for efficient and stable Sn perovskite solar cells, *ACS Energy Lett.*, 2018, **4**(1), 278–284.

29 F. Hao, C. C. Stoumpos, D. H. Cao, R. P. Chang and M. Kanatzidis, Lead-free solid-state organic–inorganic halide perovskite solar cells, *Nat. Photon.*, 2014, **8**(6), 489–494.

30 R. Fang, S. Wu, W. Chen, Z. Liu, S. Zhang, R. Chen, Y. Yue, L. Deng, Y.-B. Cheng and L. Han, [6, 6]-Phenyl-C61-butyric acid methyl ester/cerium oxide bilayer structure as efficient and stable electron transport layer for inverted perovskite solar cells, *ACS Nano*, 2018, **12**(3), 2403–2414.

31 A. Pang, J. Li, X.-F. Wei, Z.-W. Ruan, M. Yang and Z.-N. Chen, UV–$O_3$ treated annealing-free cerium oxide as electron transport layers in flexible planar perovskite solar cells, *Nanoscale Adv.*, 2020, **2**(9), 4062–4069.

32 X. Wang, L.-L. Deng, L.-Y. Wang, S.-M. Dai, Z. Xing, X.-X. Zhan, X.-Z. Lu, S.-Y. Xie, R.-B. Huang and L.-S. Zheng, Cerium oxide standing out as an electron transport layer for efficient and stable perovskite solar cells processed at low temperature, *J. Mater. Chem. A*, 2017, **5**(4), 1706–1712.

33 J. Yang, Q. Zhang, J. Xu, H. Liu, R. Qin, H. Zhai, S. Chen and M. Yuan, All-inorganic perovskite solar cells based on $CsPbIBr_2$ and metal oxide transport layers with improved stability, *Nanomaterials*, 2019, **9**(12), 1666.

34 J. Yang, J. Xu, Q. Zhang, Z. Xue, H. Liu, R. Qin, H. Zhai and M. Yuan, An efficient and stable inverted perovskite solar cell involving inorganic charge transport layers without a high temperature procedure, *RSC Adv.*, 2020, **10**(32), 18608–18613.

35 A. S. Thill, F. O. Lobato, M. O. Vaz, W. P. Fernandes, V. E. Carvalho, E. A. Soares, F. Poletto, S. R. Teixeira and F. Bernardi, Shifting the band gap from UV to visible

region in cerium oxide nanoparticles, *Appl. Surf. Sci.*, 2020, **528**, 146860.

36 C. Rodwihok, D. Wongratanaphisan, T. V. Tam, W. M. Choi, S. H. Hur and J. S. Chung, Cerium-oxide-nanoparticle-decorated zinc oxide with enhanced photocatalytic degradation of methyl orange, *Appl. Sci.*, 2020, **10**(5), 1697.

37 T. Hu, S. Xiao, H. Yang, L. Chen and Y. Chen, Cerium oxide as an efficient electron extraction layer for p–i–n structured perovskite solar cells, *Chem. Commun.*, 2018, **54**(5), 471–474.

38 I. Elango, M. Selvamani, P. C. Ramamurthy and A. V. Kesavan, Studying $V_{OC}$ in lead free inorganic perovskite photovoltaics by tuning energy bandgap and defect density, *Ceram. Int.*, 2022, **48**(19), 29414–29420.

39 F. Jannat, S. Ahmed and M. A. Alim, Performance analysis of cesium formamidinium lead mixed halide based perovskite solar cell with $MoO_x$ as hole transport material *via* SCAPS-1D, *Optik*, 2021, **228**, 166202.

40 H.-J. Du, W.-C. Wang and J.-Z. Zhu, Device simulation of lead-free $CH_3NH_3SnI_3$ perovskite solar cells with high efficiency, *Chin. Phys. B*, 2016, **25**(10), 108802.

41 P. Tiwari, M. F. Alotaibi, Y. Al-Hadeethi, V. Srivastava, B. Arkook, P. Lohia, D. K. Dwivedi, A. Umar, H. Algadi and S. Baskoutas, Design and Simulation of Efficient SnS-Based Solar Cell Using Spiro-OMeTAD as Hole Transport Layer, *Nanomaterials*, 2022, **12**(14), 2506.

42 S. M. Majeed, D. S. Ahmed and M. K. Mohammed, Anti-solvent engineering *via* potassium bromide additive for highly efficient and stable perovskite solar cells, *Org. Electron.*, 2021, **99**, 106310.

43 M. R. Mohammad, D. S. Ahmed and M. K. Mohammed, ZnO/Ag nanoparticle-decorated single-walled carbon nanotubes (SWCNTs) and their properties, *Surf. Rev. Lett.*, 2020, **27**(03), 1950123.

44 M. K. Mohammed, G. Sarusi, P. Sakthivel, G. Ravi and U. Younis, Improved stability of ambient air-processed methylammonium lead iodide using carbon nanotubes for perovskite solar cells, *Mater. Res. Bull.*, 2021, **137**, 111182.

45 R. Pandey, A. P. Saini and R. Chaujar, Numerical simulations: toward the design of 18.6% efficient and stable perovskite solar cell using reduced cerium oxide based ETL, *Vacuum*, 2019, **159**, 173–181.

46 A. Walsh, J. L. Da Silva and S.-H. Wei, Origins of band-gap renormalization in degenerately doped semiconductors, *Phys. Rev. B: Condens. Matter Mater. Phys.*, 2008, **78**(7), 075211.

47 A. Singla, R. Pandey, R. Sharma, J. Madan, K. Singh, V. K. Yadav and R. Chaujar, *Numerical Simulation of $CeO_x$ ETL based Perovskite Solar Cell: An Optimization Study for High Efficiency and Stability, 2018*, IEEE Electron Devices Kolkata Conference (EDKCON), IEEE, 2018, pp. 278–282.

48 Y. Raoui, S. Kazim, Y. Galagan, H. Ez-Zahraouy and S. Ahmad, Harnessing the potential of lead-free Sn–Ge based perovskite solar cells by unlocking the recombination channels, *Sustainable Energy Fuels*, 2021, **5**(18), 4661–4667.

49 S. Ahmmed, M. A. Karim, M. H. Rahman, A. Aktar, M. R. Islam, A. Islam and A. B. M. Ismail, Performance analysis of lead-free $CsBi_3I_{10}$-based perovskite solar cell through the numerical calculation, *Sol. Energy*, 2021, **226**, 54–63.

50 S. A. Moiz, Optimization of hole and electron transport layer for highly efficient lead-free $Cs_2TiBr_6$-based perovskite solar cell, *Photonics*, 2021, 23.